

CHAPTER 4

VERTICAL SIDE SHEAR AND POINT RESISTANCE OF PILE/SHAFT IN SAND

4.1 INTRODUCTION

The friction pile in cohesionless soil gains its support from the pile tip resistance and the transfer of load via the pile wall along its length. It has been suggested that the load transferred by skin friction pile can be neglected which is not always the case. The load transferred via the pile wall depends on the diameter and length of the pile, the surface roughness, and soil properties. It should also be mentioned that both pile point and skin resistances are interdependent.

The assessment of the mobilized load transfer of a pile in sand depends on the success in developing a representative t-z relationship. This can be achieved via empirical relationships (Kraft et al. 1981) or numerical methods (Randolph and Worth, 1978). The semi-empirical procedure presented in this chapter employs the stress-strain relationship of sand and findings from experimental tests. The t-z curve obtained based on the current study will be used in Chapter 5 to account for the vertical side shear resistance that develops with the laterally loaded large diameter shafts.

The method of slices presented in this chapter reflects the analytical portion of this technique that allows the assessment of the attenuating shear stress/strain and vertical displacement within the vicinity of the driven pile. As a result, the load transfer and the t-z curve can be assessed using a combination between the tip and side resistances of the pile.

PILE POINT (SHAFT BASE) RESISTANCE AND SETTLEMENT

$(Q_P - z_P)$ IN SAND

It is evident that the associated pile tip resistance manipulates the side resistance of the pile shaft. As presented in the analysis procedure, the pile tip resistance should be assumed at the first step. As a result, the shear resistance and displacement of the upper segments of the pile can be

computed based on the assumed pile tip movement. This indicates the need for a practical technique that allows the assessment of the pile tip load-displacement relationship under a mobilized or developing state. Most of the available techniques provide the ultimate pile tip resistance that is independent of the specified settlement. In other words, the pile tip settlement at the ultimate tip resistance is a function of the pile diameter (e.g. 5 to 10% of pile tip diameter). Thereafter, a hyperbolic curve is used to describe the load-settlement curve based on the estimated ultimate resistance and settlement of the pile tip.

Elfass (2001) developed an approach that allows the assessment of the mobilized pile tip resistance in sand and the accompanying settlement over the whole range of soil strain up to and beyond soil failure. In association with the pile side shear resistance technique presented in Section 4-2, the approach established by Elfass (2001) will be employed in the current study to compute the pile tip load-settlement in sand.

The failure mechanism developed by Elfass (2001) assumes four failure zones represented by four Mohr circles as shown in Fig. 4.1. This mechanism yields the bearing capacity (q) and its relationship with the deviatoric stress (σ_d) of the last (fourth Mohr circle) as shown in Fig 4-2. .

$$\mathbf{s}_d = 0.6 q \quad (4-1)$$

The pile tip resistance (Q_P) is given as,

$$Q_P = q A_{base} = \frac{\mathbf{s}_d}{0.6} A_{base} \quad (4-2)$$

where A_{base} is the cross sectional area of the pile tip (shaft base).

As seen in Fig. 4-1, the Mohr Columb strength envelope is nonlinear and requires the evaluation of the secant angle of the fourth circle (ϕ_{IV}) tangent to the curvilinear envelope. The angle of the secant line tangent to first circle (ϕ_I) at effective overburden pressure can be obtained from the field blow data count (SPT test) or a laboratory triaxial test at approximately 1 tsf (100 kPa) confining pressure. Due to the increase in the confining pressure ($\bar{\mathbf{s}}_3$) from one circle to the

next, the friction angle (ϕ) decreases from ϕ_I at $(\bar{\mathbf{s}}_3)_I$ to ϕ_{IV} at $(\bar{\mathbf{s}}_3)_{IV}$ based on the following Bolton (1986) relationship modified by Elfass (2001) (Fig. 4-3)

$$\mathbf{j}_{peak} = \mathbf{j}_{min} + \mathbf{j}_{diff} \quad (4-3)$$

$$\mathbf{j}_{diff} = 3I_R = 3D_R \left\{ 10 - \ln \left[\left(\frac{2 + \tan^2(45 + \mathbf{j}/2)}{3} \right) \bar{\mathbf{s}}_3 \right] \right\} - 1 \quad (4-4)$$

$\bar{\mathbf{s}}_3$ is in kPa. ϕ_{min} is the lowest friction angle that ϕ may reach at high confining pressure, as shown in Fig. 4-4 and D_r is inputted as its decimal value.

Knowing the sand relative density (D_r) and the associated friction angle under the original confining pressure ($\bar{\mathbf{s}}_3 = \bar{\mathbf{s}}_{vo}$), the reduction in the friction angle ($\Delta\phi$) due to the increase of the confining pressure from $\bar{\mathbf{s}}_{vo}$ to $(\bar{\mathbf{s}}_3)_{IV}$ can be evaluated based on Eqns. 4-3 and 4-4, as described in the following steps:

1. Based on Eqn. 4-4, calculate $(\phi_{diff})_I$ at the original confining pressure ($\bar{\mathbf{s}}_3 = \bar{\mathbf{s}}_{vo}$)

$$(\mathbf{j}_{diff})_I = 3D_R \left\{ 10 - \ln \left[\left(\frac{2 + \tan^2(45 + \mathbf{j}_I/2)}{3} \right) \bar{\mathbf{s}}_{vo} \right] \right\} - 1 \quad (4-5)$$

2. Assume a value for the deviatoric stress (σ_d) of the fourth circle (Fig. 4-2). As a result,

$$q = \frac{\mathbf{s}_d}{0.6} \quad (4-6)$$

$$(\bar{\mathbf{s}}_3)_{IV} = \bar{\mathbf{s}}_{vo} + q - \mathbf{s}_d = \bar{\mathbf{s}}_{vo} + 0.4q \quad (4-7)$$

3. Assume a reduction ($\Delta\phi = 3$ or 4 degrees) in the sand friction angle at ($\bar{\mathbf{s}}_3 = \bar{\mathbf{s}}_{vo}$) due to the increase in the confining pressure from $\bar{\mathbf{s}}_{vo}$ to $(\bar{\mathbf{s}}_3)_{IV}$, as seen in Fig. 4-4. Therefore,

$$\phi_{IV} = \phi_I - \Delta\phi \quad (4-8)$$

4. As presented by Elfass (2001) and shown in Fig. 4-4, ϕ changes in a linear pattern with the logarithmic increase of $\bar{\mathbf{s}}_3$. The friction angle ϕ_{IV} associated with the confining pressure $(\bar{\mathbf{s}}_3)_{IV}$ can be calculated as

$$\mathbf{j}_{IV} = \mathbf{j}_I - \Delta\mathbf{j} \log \frac{(\bar{\mathbf{s}}_3)_{IV}}{\mathbf{s}_{vo}} \quad (4-9)$$

5. According to the computed friction angle (ϕ_{IV}) , use Eqn. 4-4 to evaluate $(\phi_{diff})_{IV}$.

$$(\mathbf{j}_{diff})_{VI} = 3D_R \left[10 - \ln \left[\left(\frac{2 + \tan^2(45 + \mathbf{j}_{IV}/2)}{3} \right) (\bar{\mathbf{s}}_3)_{IV} \right] - 1 \right] \quad (4-10)$$

6. Having the values of $(\phi_{diff})_I$ and $(\phi_{diff})_{IV}$, a revised value for $\Delta\phi$ can be obtained.

$$\Delta\phi = (\phi_{diff})_I - (\phi_{diff})_{IV} \quad (4-11)$$

7. Compare the value of $\Delta\phi$ obtained in step 6 with the assumed $\Delta\phi$ in step 3. If they are different, take the new value and repeat the steps 3 through 7 until the value of ϕ_{IV} converges and the difference in $\Delta\phi$ reached is within the targeted tolerance.

8. Using the calculated values of ϕ_I and ϕ_{IV} , the deviatoric stress at failure can be expressed as

$$\mathbf{s}_{df} = (\bar{\mathbf{s}}_3)_{IV} \left(\tan^2(45 + \mathbf{j}_{IV}/2) - 1 \right) \quad (4-12)$$

9. The current stress level (SL) in soil (Zone 4 below pile tip) is evaluated as

$$SL = \frac{\tan^2(45 + \mathbf{j}_m/2) - 1}{\tan^2(45 + \mathbf{j}_{IV}/2) - 1} = \frac{\mathbf{s}_d}{\mathbf{s}_{df}} \quad ; \quad \mathbf{s}_d = SL \mathbf{s}_{df} \quad (4-13)$$

where

$$\mathbf{j}_m = \sin^{-1} \left(\frac{\mathbf{s}_d/2}{(\bar{\mathbf{s}}_3)_{IV} + \mathbf{s}_d/2} \right) \quad (4-14)$$

4.2.1 Pile Tip Settlement

As presented in Chapter 3 with clay soil, the pile tip displacement in sand can be determined based on the drained stress-strain relationship presented in Chapter 5 (Norris 1986 and Ashour et al. 1998). The soil strain (ϵ) below the pile tip is evaluated according to the following equations: Corresponding to a triaxial test at a given confining pressure (\bar{s}_3) at a deviator stress (σ_d) and stress level (SL) as given by Eqns. 4-12 through 4-14.

$$\mathbf{e} = \frac{SL e^{3.707 SL}}{\mathbf{I}} \mathbf{e}_{50} \quad (4-15)$$

The value 3.707 and λ represent the fitting parameters of the power function relationship, and ϵ_{50} symbolizes the soil strain at 50 percent stress level. λ is equal to 3.19 for SL less than 0.5 and λ decreases linearly with SL from 3.19 at 0.5 to 2.14 at SL equal to 0.8.

Equation 4-16 represents the final loading zone which extends from 80 percent to 100 percent stress level. The following equation is used to assess the strain (ϵ) in this range:

$$SL = \exp \left[\ln 0.2 + \frac{100 \mathbf{e}}{(m \mathbf{e} + q)} \right] ; \quad SL \geq 0.80 \quad (4-16)$$

where $m=59.0$ and $q=95.4 \epsilon_{50}$ are the required values of the fitting parameters.

The two relationships mentioned above are developed based on unpublished experimental results (Norris 1977).

For a constant Young's modulus (E) with depth, the strain or ϵ_1 profile has the same shape as the elastic ($\Delta\sigma_1 - \Delta\sigma_3$) variation or Schmertmann's I_z factor (Schmertmann 1970, Schmertmann et al. 1979 and Norris 1986). Taking ϵ_1 at depth B/2 below the shaft base (the peak of the I_z curve), the shaft base displacement (z_p) is a function of the area of the triangular variation (Fig. 3-9).

$$z_p = e B \quad (4-17)$$

where B is the diameter of the pile point (shaft base). Dealing with different values for pile tip resistance (Eqn. 4-2), the associated deviatoric stress (Eqn. 4-1), stress level (Eqn. 4-13) and principal strain (ϵ) (Eqns. 4-15 and 4-16) can be used to assess base movement in order to construct the pile tip load-settlement ($Q_p - z_p$) curve.

4.2 LOAD TRANSFER ALONG THE PILE/SHAFT SIDE (VERTICAL SIDE SHEAR)

4.3.1 Method of Slices for Calculating the Shear Deformation and Vertical Displacement in Cohesionless Soil

The methodology presented in this chapter is called the method of slices. The soil around the pile/shaft is modeled as soil horizontal slices that deform vertically as shown in Fig. 4-5. The shear stress/strain caused by the shaft settlement (z) at a particular depth gradually decreases along the radial distance (r) from the pile wall. As seen in Fig. 4-6, the shear stress (τ) and strain (γ) experience their largest values (τ_{\max} and γ_{\max}) just at the contact surface between the shaft and the adjacent sand. Due to the shear resistance of sand, the induced shear stress/ strain decreases to zero and large radial distance (r).

Randolph and Worth (1978) and Kraft et al. (1981) assume the shear stress decreases with distance such that $\tau r = \tau_o r_o$ in which τ_o is the shear stress (τ_{\max}) at the pile wall (r_o); and τ is the shear stress angular ring at distance r . However, Randolph and Worth (1978) argued this assumption and indicated that the shear stress decreases rapidly with the distance r . Based on this assumption, Terzaghi (1943) showed a more decreasing parabolic pattern (similar to the one shown in Fig. 4-7) for the horizontal variation of the shear stress caused by the axially loaded sheet pile embedded in a homogenous mass of soil. Robinsky and Morrison (1964) performed experimental tests on model piles embedded in sand that exhibited the parabolic deflection pattern seen in Fig. 4-7. The following relationship describes the attenuation in the shear stress (τ) in soil with the distance r for such a parabolic pattern.

$$\frac{\mathbf{t}}{\mathbf{t}_o} = \frac{r_o^2}{r^2} \quad (4-18)$$

In order to understand the slice method, the stress-strain conditions of a small soil element at the contact surface with the pile shaft is analyzed. Figure 4-8 shows the induced shear stress on the soil-pile contact surface.

The lateral earth pressure coefficient (K) varies, with the radial distance, from 1 at the pile wall (due to pile installation) to $K = K_o = 1 - \sin \phi$ in the free-field where the z-movement-induced shear stress (τ) reaches zero. Therefore, the horizontal effective stress at the pile wall after installation (prior to loading of the pile) just equals the vertical effective overburden, $\bar{\mathbf{s}}_{vo}$ (i.e. lateral earth pressure coefficient $K = 1$). It should be noted that τ_o represents the τ_{\max} induced at the pile wall. Accordingly, a Mohr circle with a center at $\bar{\mathbf{s}}_{vo}$ and a diameter of $2\tau_o$ ($\tau_{\max} = \tau_o$) develops at $r = r_o$, as shown in Fig. 4-8. With radial distance from the pile, the horizontal normal stress (σ_h) and the deviator stress (σ_d) continue to drop from $\bar{\mathbf{s}}_{vo}$ and $2\tau_{\max}$ at r_o to $\bar{\mathbf{s}}_{vo} (1 - \sin \mathbf{j})$ and $\bar{\mathbf{s}}_{vo} (1 - K_o)$ or $\bar{\mathbf{s}}_{vo} \sin \mathbf{j}$ in the far-field (where τ due to z is 0). The corresponding shear strain ($\gamma = \gamma_{\max}$) causes a major normal strain ϵ_1 ,

$$\epsilon_1 = (1 + \nu) \gamma \quad (4-19)$$

In addition, the shear modulus (G) is related to the Young's modulus (E) at the given effective confining pressure ($\bar{\mathbf{s}}_3$) and normal strain (ϵ_1), i.e.

$$G = \frac{E}{2(1 + \mathbf{n})} \quad (4-20)$$

The method of slices described in Fig. 4-10, is based on the shear stress variation concepts presented above. The proposed method of slices provides the radius of the soil ring (radial distance, r) over which the induced shear stress diminishes, as shown in Fig. 4-7.

As shown in Fig. 4-11 for soil ring 1, the horizontal stress (σ_h) on the soil-pile interface (inner surface of the first soil slice) is equal to \bar{s}_{vo} . At the same time, the horizontal stress (σ_h) on the outer surface is expressed as

$$s_h = \bar{s}_{vo} - \Delta t \quad (4-21)$$

The horizontal (radial and tangential) equilibrium is based on the ring action for the whole ring of soil ($2\pi r$) around the pile. The vertical equilibrium is also conducted on a full ring of soil. The vertical equilibrium of the first soil ring (slice) adjacent to the pile wall is expressed by the following equations:

$$\sum F_y = 0 \quad (4-22)$$

$$R_B \cos \mathbf{j}_B - R_T \cos \mathbf{j}_T - \Delta T - W_1 = 0 \quad (4-23)$$

Therefore,

$$R_B \cos \mathbf{j}_B - R_T \cos \mathbf{j}_T - \Delta T - W_1 = 0 \quad (4-24)$$

and

$$W_1 = R_B \cos \mathbf{j}_B - R_T \cos \mathbf{j}_T - \Delta T \quad (4-25)$$

where ΔT represents the reduction in the vertical shear force along the radial width (Δr) of the horizontal soil ring.

The following steps explain the implementation of the method of slices:

1. Divide the pile length into a number of segments that are equal in length (H_s). Note that the effective stress (\bar{s}_{vo}) (i.e. the initial confining stress) increases with depth for each pile segment.
2. Assume a shear stress developed at the soil-pile interface ($r = r_o$) equal to that at soil failure or τ_{ult} . It should be noted that there might be a slip condition (e.g. $\tau_{limit} = K \bar{s}_{vo} \tan \delta$) at the soil pile interface that limits to a value τ_{limit} less than τ_{ult} .

3. Determine the developing confining pressure \bar{s}_3 due to τ_{\max} (Fig. 4-11)

$$\bar{s}_3 = K_o \bar{s}_{vo} = 1 - \sin j \quad (4-26)$$

where φ the friction angle at failure.

4. Increase the radial distance (r) from r_o to r_1 by a small incremental amount (Δr). As a result, the vertical shear stress on the face of the slice at r_1 will drop to τ_1 as expressed in Eqn. 4-21.
5. The horizontal stress (σ_h) on the vertical face of the soil slice decreases with the attenuating shear stress (τ) as shown in Fig. 4-9 until it reaches the value of \bar{s}_3 given in Eqn. 4-26. The Mohr circles shown in Fig. 4 describe the decrease in horizontal stress (σ_h) and the mobilized friction angle (φ_m) in association to the attenuation in the shear stress (τ) (and the vertical shear force, T , on a vertical unit length) acting on the vertical face of the soil ring, i.e.

$$\Delta T_1 = T_0 - T_1 = 2\pi (r_o \tau_o - r_1 \tau_1) \quad (4-27)$$

$$R_T = \frac{\bar{s}_{hl}}{\cos j_T} p (r_1^2 - r_o^2) \quad (4-28)$$

$$R_B = \frac{\bar{s}_{vo}}{\cos j_B} p (r_1^2 - r_o^2) \quad (4-29)$$

It should be noted that \bar{s}_{vo} is the effective stress at the middle of the slice which is used as an average effective stress for the whole slice (i.e. with More circle). The angles φ_T and φ_B at the top and bottom of the first soil ring, respectively, are determined as follows,

$$j_B = \sin^{-1} \frac{t_o}{s_{vo}} \quad (4-30)$$

$$j_T = \sin^{-1} \frac{t_1}{s_{vo} - \Delta t} \quad \text{where } \Delta t = t_o - t_1 \quad (4-31)$$

ϕ_B equals ϕ_T of the next slice (soil ring 2) where τ_1 and τ_2 are the vertical shear stresses at radii r_1 and r_2 , respectively (Fig. 4-12).

6. Based on the induced shear stress (τ_o) on the inner face of the current soil ring (first ring) and its Mohr circle, calculate the associated shear strain (γ) that develop over the width (Δr) of the current soil ring. For each horizontal soil slice i (soil ring with a width Δr) and based on the induced shear stress (τ) as seen in Fig. 4-10, the normal strain and stress (ϵ and σ_d), and v will be evaluated. Thereafter, determine the associating shear strain γ_i and vertical displacement z_i as follows,

$$\mathbf{g}_i = \frac{\mathbf{e}_i}{1 + \mathbf{n}} \quad (4-32)$$

where

$$\mathbf{n} = 0.1 + 0.4 SL_i$$

$$z_i = \mathbf{g}_i \Delta r_i \quad (4-33)$$

7. Repeat steps 1 through 6 for larger values of r (i.e. an additional soil ring) and calculate z_i for each soil slice (ring) until the induced vertical shear stress approaches zero at $r = r_f$.
8. Assess the total vertical displacement at the soil-pile contact ($\tau = \tau_{\max}$ or τ_o) as follows,

$$z_f = \sum_{t=\tau_o}^{t=0} z_i \quad (4-34)$$

z_f represents the elastic vertical displacement at failure at the soil-pile contact that is needed to construct the Ramberg-Osgood model in the next sections.

It would be noticed that the soil ring is always in horizontal equilibrium. For example, the horizontal equilibrium for the first ring of soil can be expressed as

$$\sum F_x = 0$$

$$E_o + R_T \sin \mathbf{j}_T - E_1 - R_B \sin \mathbf{j}_B = 0 \quad (4-35)$$

where,

$$E_o = \bar{\mathbf{s}}_{vo} 2\mathbf{p}_o H_s \quad (4-37)$$

$$E_1 = \bar{\mathbf{s}}_v 2\mathbf{p}_1 H_s \quad (4-38)$$

$\bar{\mathbf{s}}_v$ varies from $\bar{\mathbf{s}}_{vo}$ at the sand-pile contact surface to $\bar{\mathbf{s}}_{vo} (1 - \sin \mathbf{j})$ at r_f where the induced shear stress (τ) = 0, as shown in Fig. 4-7.

4.3.2 Ramberg-Osgood Model for Sand

As presented in Chapter 3 with the clay soil, Ramberg-Osgood model represented by Eqn. 4-39 can be used to characterize the t-z curve.

$$\frac{z}{z_r} = \frac{\mathbf{g}}{\mathbf{g}_r} = \frac{\mathbf{t}}{\mathbf{t}_{ult}} \left[1 + \mathbf{b} \left(\frac{\mathbf{t}}{\mathbf{t}_{ult}} \right)^{R-1} \right] \quad (4-39)$$

At $\tau/\tau_{ult} = 1$ then

$$\mathbf{b} = \frac{\mathbf{g}_f}{\mathbf{g}_r} - 1 \quad (4-40)$$

At $\tau/\tau_{ult} = 0.5$ and $\gamma = \gamma_{50}$, then

$$R-1 = \frac{\log \frac{2 \frac{\mathbf{g}_{50}}{\mathbf{g}_r} - 1}{\mathbf{b}}}{\log (0.5)} = \frac{\log \frac{2 \frac{\mathbf{g}_{50}}{\mathbf{g}_r} - 1}{\frac{\mathbf{g}_f}{\mathbf{g}_r} - 1}}{\log (0.5)} \quad (4-41)$$

The initial shear modulus (G_i) at a very low SL and the shear modulus (G_{50}) at SL = 0.5 can be determined via their direct relationship with the normal stress-strain relationship and Poisson's ration (ν)

$$G_i = \frac{E_i}{2(1+n)} = \frac{E_i}{2.2} \quad \nu \text{ for sand} = 0.1 \quad (4-42)$$

and

$$G_{50} = \frac{E_{50}}{2(1+n)} = \frac{E_{50}}{3} = \frac{\mathbf{s}_{df}/2}{3 \mathbf{e}_{50}} \quad (4-43)$$

Therefore,

$$\mathbf{g}_r = \frac{\mathbf{t}_{ult}}{G_i} = \frac{\mathbf{s}_{df}/2}{G_i} \quad (4-44)$$

The Poisson's ratio (ν) for sand varies 0.1 to 0.5 with the increasing values of SL as follows,

$$\mathbf{n} = 0.1 + 0.4 SL \quad (4-45)$$

The shear strain at failure (γ_f) is determined in terms of the normal strain at failure (ϵ_f).

$$\mathbf{g}_f = \frac{\mathbf{e}_f}{(1+n)} = \frac{\mathbf{e}_f}{1.5} \quad (4-46)$$

The normal stress-strain relationship of sand ($\sigma_d - \epsilon$) is assessed based on the procedure presented in Chapter 5. The initial Young's modulus of clay (E_i) is determined at a very small value of the normal strain (ϵ) or stress level (SL). In the same fashion, ϵ_f is evaluated at SL = 1 or the normal strength σ_{df} . By knowing the values of γ_r , γ_{50} and γ_f , the constants β and R of the Ramberg-Osgood model shown in Eqn. 4-39 can be evaluated.

The Ramberg-Osgood model given in Eqn. 4-39 allows the assessment of the elastic vertical displacement that occurs at the soil-pile contact surface based on z_f obtained in Section 4-3-1. Equation 4-39 can be rewritten as follows,

$$\frac{z}{z_r} = \frac{\mathbf{t}}{\mathbf{t}_{ult}} \left[1 + \mathbf{b} \left(\frac{\mathbf{t}}{\mathbf{t}_{ult}} \right)^{R-1} \right] \quad (4-47)$$

where,

$$\frac{z_r}{z_f} = \frac{g_r}{g_f} \quad i.e. \quad z_r = z_f \frac{g_r}{g_f} \quad (4-48)$$

4.3.3 Procedure Steps to Assess Load Transfer and Pile Settlement in Sand (t-z Curve)

The assessment of the load transfer and associated settlement of a pile embedded in sand requires the employment of t-z curve for that particular soil. The load transferred from pile shaft to the surrounding sand is a function of the diameter and the surface roughness of the pile skin and sand properties (effective unit weight, friction angle, relative density and confining pressure) in addition to the pile tip resistance. The development of a representative procedure allows the assessment of the t-z curve in soil (sand and/or clay) that leads to the prediction of a nonlinear load-settlement curve at the pile/shaft head. Such a relationship provides the mobilized pile-head settlement under axial load and vertical shear resistance.

A new procedure is developed in this chapter to assess pile/shaft skin resistance in sand in a mobilized fashion. The proposed procedure provides the deformation in sand around the pile in the radial zone affected by the pile movement (Fig. 4-1). At the same time, the horizontal degradation (attenuation) of the shear stress away from the pile is evaluated by the suggested analysis. As a result, the varying shear stress/strain, shear modulus and deformation in the radial distance away from the pile can be predicted based on reasonable assumptions.

The presented t-z curve is developed according to the induced displacement along the pile. The following steps present the procedure that is employed to assess the load transfer and pile movement in sand soil:

1. Based on the approach presented in Section 4-2 for the pile tip resistance, assume a small pile tip resistance, Q_p as given in Eqns (4-1 and 4-2)

2. Using the SL evaluated above and the stress-strain relationship presented in Eqns. 4-13 through 4-16, compute the induced axial (deviatoric) soil strain, ϵ_P and the shaft base displacement, $z_P = \epsilon_P B$. B is the diameter of the shaft base.
3. Divide the pile length into segments equal in length (h_s). Take the load Q_B at the base of the bottom segment as (Q_P) and movement at its base (z_B) equal to (z_P). Estimate a midpoint movement for the bottom segment (segment 4 as seen in Fig. 4-13). For the first trial, the midpoint movement can be assumed equal to the shaft base movement.
4. Calculate the elastic axial deformation of the bottom half of this segment,

$$z_{\text{elastic}} = \frac{Q_B h_s / 2}{EA_{\text{base}}} \quad (4-49)$$

The total movement of the midpoint in the bottom segment (segment 4) is equal to

$$z = z_T + z_{\text{elastic}} \quad (4-50)$$

5. Based on the soil properties of the surrounding sand, use a Ramberg-Osgood formula to characterize the backbone response (Richart 1975).

$$\frac{z}{z_r} = \frac{\mathbf{g}}{\mathbf{g}_r} = \frac{\mathbf{t}}{\mathbf{t}_{ult}} \left[1 + \mathbf{b} \left(\frac{\mathbf{t}}{\mathbf{t}_{ult}} \right)^{R-1} \right] \quad (4-51)$$

z = total midpoint movement of a pile/shaft segment

γ = average shear strain in soil adjacent to the shaft segment

τ = average shear stress in soil adjacent to the shaft segment

γ_r is the reference strain, as shown in Fig. 3-4, and given by Eqn. 4-44

z_r = shaft segment movement associated to γ_r

ϵ_{50} = axial strain at SL = 0.5. ϵ_{50} can be obtained from the chart provided in Chapter 5.

β and $R-1$ are the fitting parameters of the Ramberg-Osgood model given in Eqn. 4-52. These parameters are evaluated in section 4.2.1.

6. Using Eqn. 4-51 which is rewritten in the form of Eqn. 4-52, the average shear stress level (SL_t) in sand around the shaft segment can be obtained iteratively based on movement z evaluated in Eqn. 4-50.

$$\frac{z}{z_r} = \frac{\mathbf{g}}{\mathbf{g}_r} = SL_t \left[1 + \mathbf{b}(SL_t)^{R-1} \right] \quad (\text{Solved for } SL_t) \quad (4-52)$$

7. Shear stress at soil-shaft contact surface is then calculated, i.e.

$$\tau = SL \sigma_{df}/2 \quad (4-53)$$

8. The axial load carried by the shaft segment in skin friction / adhesion (Q_s) is expressed as

$$Q_s = \pi B h_s \tau \quad (4-54)$$

9. Calculate the total axial load (Q_i) carried at the top of the bottom segment ($i = 4$).

$$Q_i = Q_s + Q_B \quad (4-55)$$

10. Determine the elastic deformation in the bottom half of the bottom segment assuming a linear variation of the load distribution along the segment.

$$Q_{mid} = (Q_i + Q_B) / 2 \quad (4-56)$$

$$z_{elastic} = \left(\frac{Q_{mid} + Q_B}{2} h_s \right) / EA = \frac{(Q_i + 3 Q_B) h_s}{8EA} \quad (4-57)$$

11. Compute the new midpoint movement of the bottom segment.

$$z = z_p + z_{\text{elastic}} \quad (4-58)$$

12. Compare the z value calculated from step 11 with the previously evaluated estimated movement of the midpoint from step 4 and check the tolerance.
14. Repeat steps 4 through 12 using the new values of z and Q_{mid} until convergence is achieved
15. Calculate the movement at the top of the segment $i=4$ as

$$z_i = z_B + \frac{Q_i + Q_B}{2} \frac{h_s}{AE}$$

16. The load at the base (Q_B) of segment $i=3$ is taken equal to Q_4 (i.e. Q_{i+1}) while z_B of segment 3 is taken equal to z_4 and steps 4-13 are repeated until convergence for segment 3 is obtained. This procedure is repeated for successive segments going up until reaching the top of the pile where pile head load Q is Q_1 and pile top movement δ is z_1 . Based on presented procedure, a set of pile-head load-settlement coordinate values ($Q - \delta$) can be obtained on coordinate pair for each assumed value of Q_T . As a result the load transferred to the soil along the length of the pile can be calculated for any load increment.
17. Knowing the shear stress (τ) and the associated displacement at each depth (i.e. the midpoint of the pile segment), points on the t - z curve can be assessed at each new load.

4.4 PROCEDURE VALIDATION

As reported by Vesic (1970), an 18-inch diameter steel pipe pile with 0.5-inch-thick walls was driven and tested in five stages. The bottom section has a 2-in thick flat steel plate at the base of the pile. Tests with this pile were performed at driving depths of 10, 20, 30, 40 and 50 ft. Figure, 4-14 shows the results of the standard penetration tests (SPT) at different locations at the test site. Figure 4-15 the particle size distribution curves of two different types of sands. The

fine sand curves in this figure refer to the material found mostly at the top 5 ft of the soil profile. It should be noted that the frictions angles shown in Table 4-1 is a little bit relatively high compared to the associated $(N_1)_{60}$.

Table 4-1 – Suggested Soil Data for Current Soil Profile

Soil layer #	Soil type	Thickness (ft)	γ (pcf)	$(N_1)_{60}$	ϕ (deg.)	ϵ_{50}^{**}
1	Sand	10	110	9	30	0.009
2	Sand	10	60	15	32	0.007
3	Sand	10	60	19	35	.006
4	Sand	10	66	24	39	.004
5	Sand	10	66	32	42	0.003

Figure 4-16 exhibits a comparison between the measured and computed data at the depths 20, 40 and 50 ft below ground. Good agreement between the measured and computed axial pile load can be seen in Fig. 4-16.

4.5 SUMMARY

This Chapter presents a procedure that allows the assessment of the t-z and load-settlement curves for a pile in sand. The methodology employed is based on the elastic theory, stress-strain relationship, and the method of slices for the vertical equilibrium. The results obtained incorporate the pile tip and side resistance in a mobilized fashion. The results obtained in comparison with the field data show the capability of the suggested technique. The findings of this chapter will be employed in Chapter 5 to evaluate the vertical side shear resistance induced by the lateral deflection of a large diameter shaft and its contribution to the lateral resistance of the shaft.

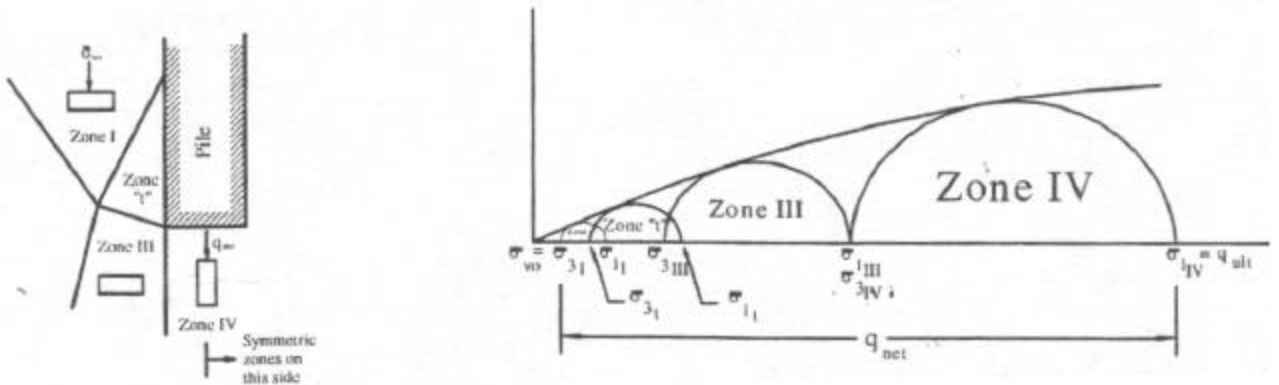


Fig. 4-1 Failure Mechanism of Sand Around Pile Tip (Elfass, 2001)

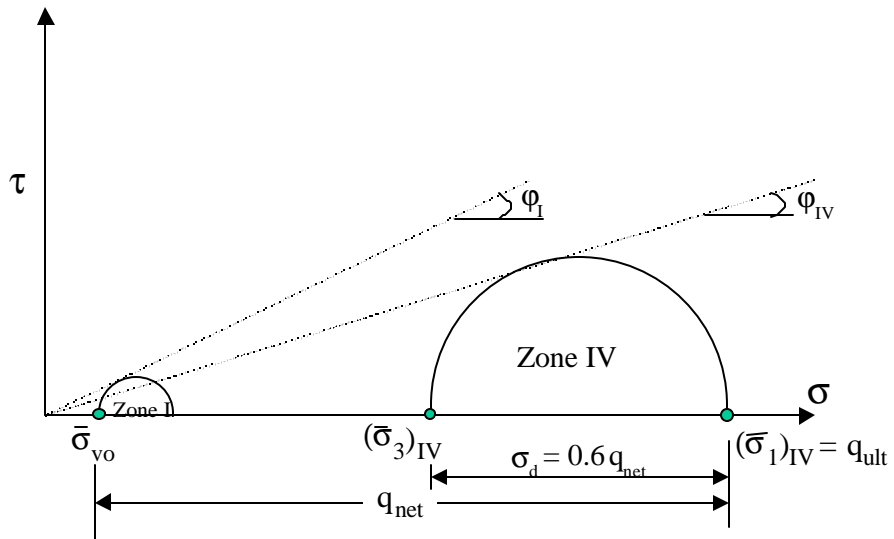


Fig. 4-2 Relationship Between Bearing Capacity (q_{net}) of Pile Tip in Sand and the Deviatoric Stress (σ_d) (after Elfass, 2001)

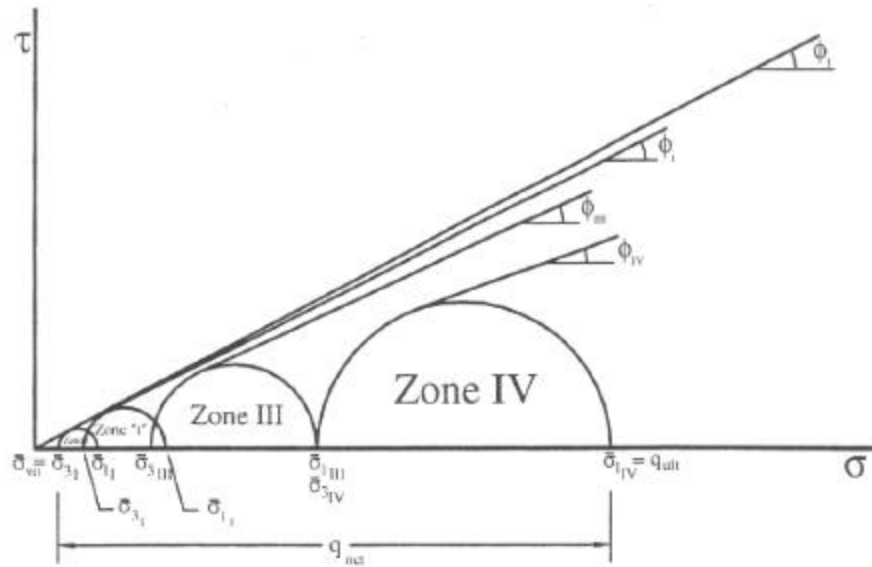


Fig. 4-3 Degradation in the Secant Friction Angles of Circles Tangent to a Curvilinear Envelope of Sand Due to the Increase in the Confining Pressure (Elfass, 2001)

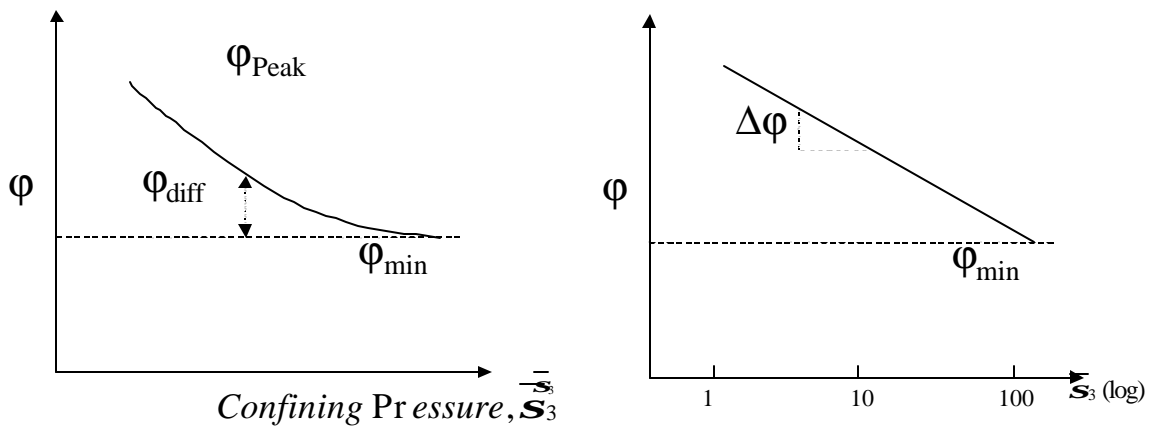


Fig. 4-4 Changes of Friction Angle (ϕ) with the Confining Pressure

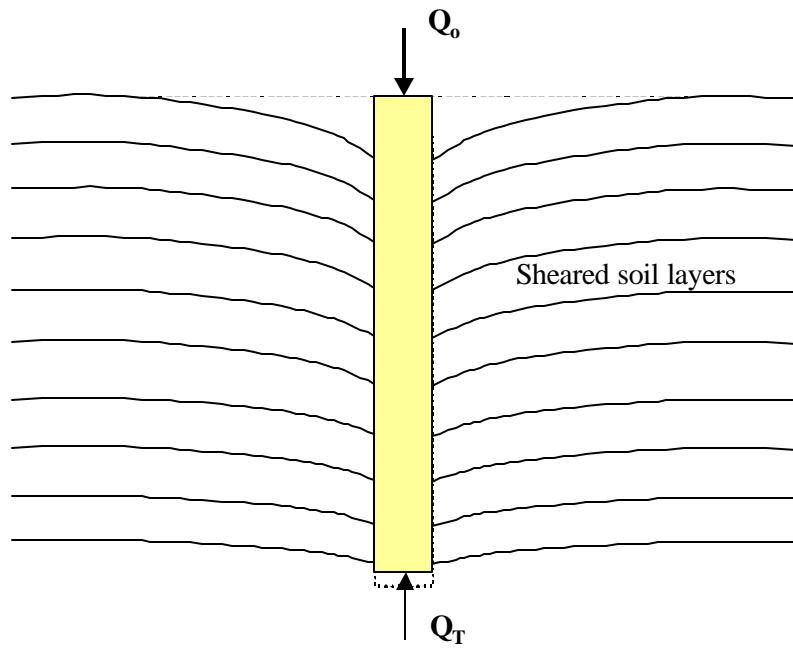


Fig. 4-5 Soil Deformation in the Vicinity of Axially Loaded Pile.

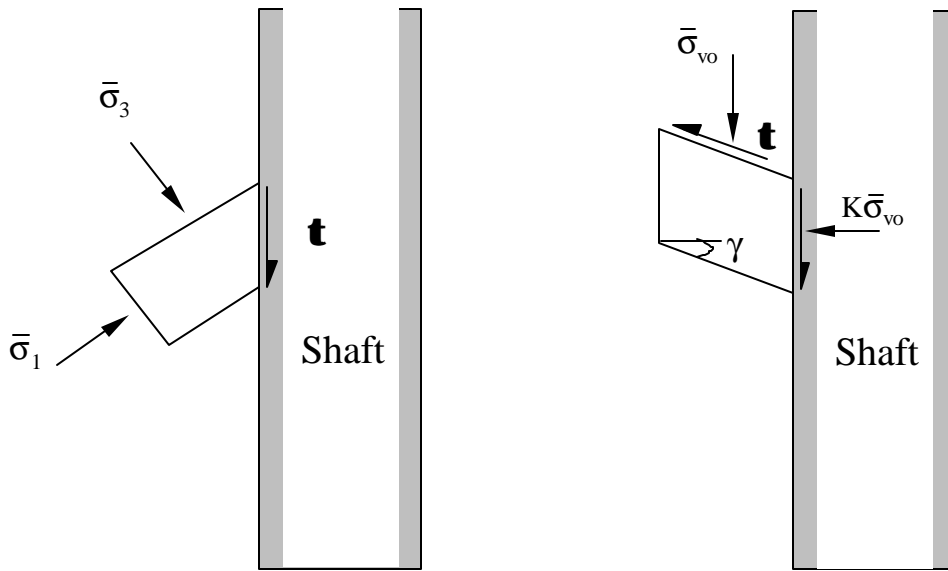


Fig. 4-6 Shear Stress/Strain at Soil-Pile Interface.

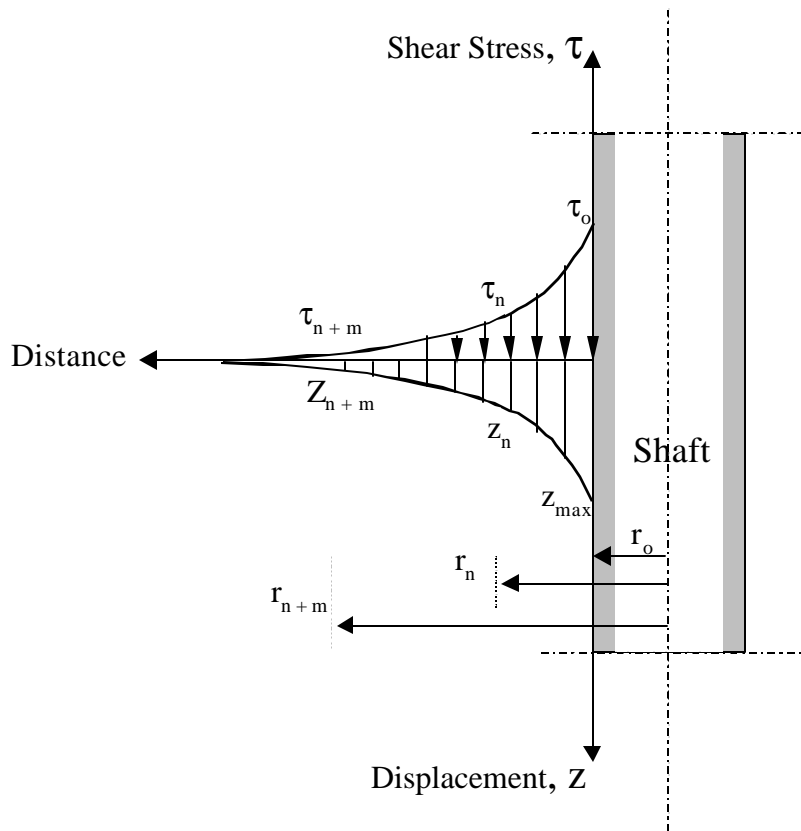


Fig. 4-7 Shear and Displacement Attenuation with the Radial Distance from the Pile Wall.

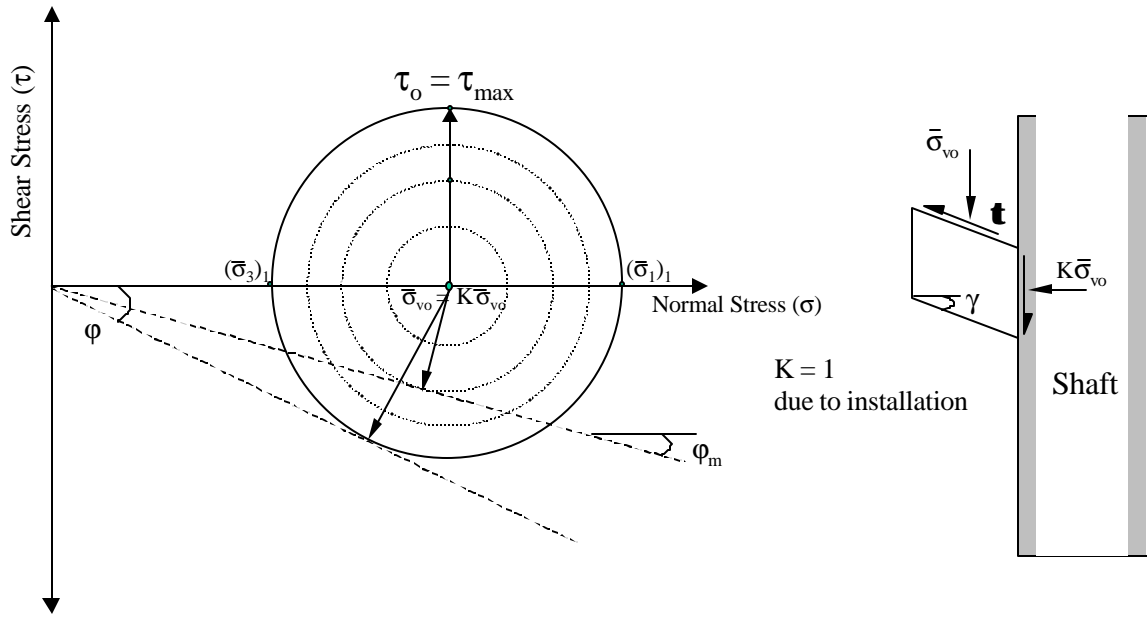


Fig. 4-8 Growth of Shear Stress at the Soil-Pile Contact Surface (Pile Wall) Due to Pile Movement

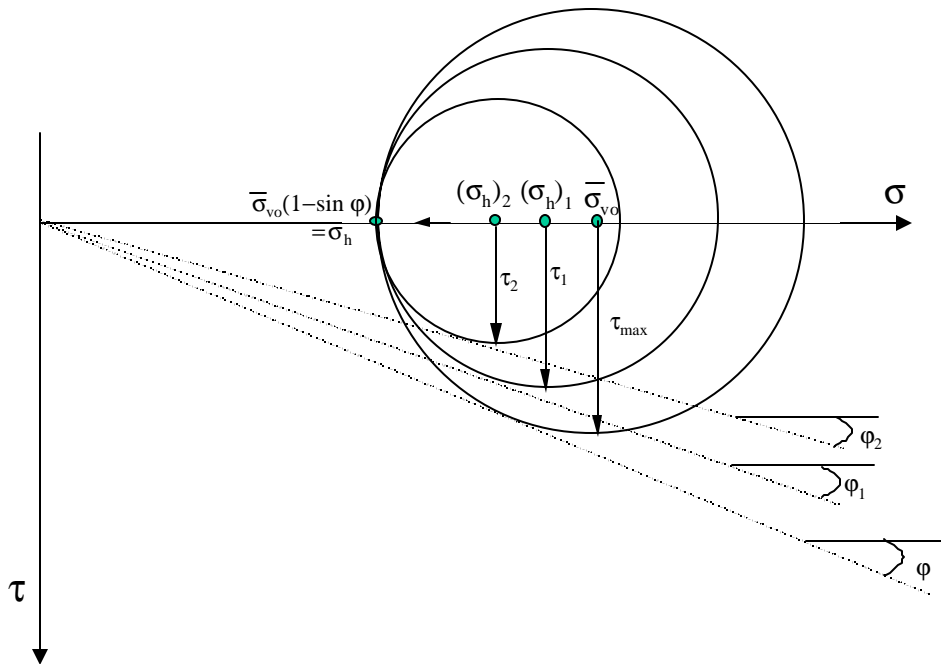


Fig. 4-9 Mohr Circles that Represent the Radial Attenuation of Shear and Normal Stresses For a Given Displacement z at the Pile Wall

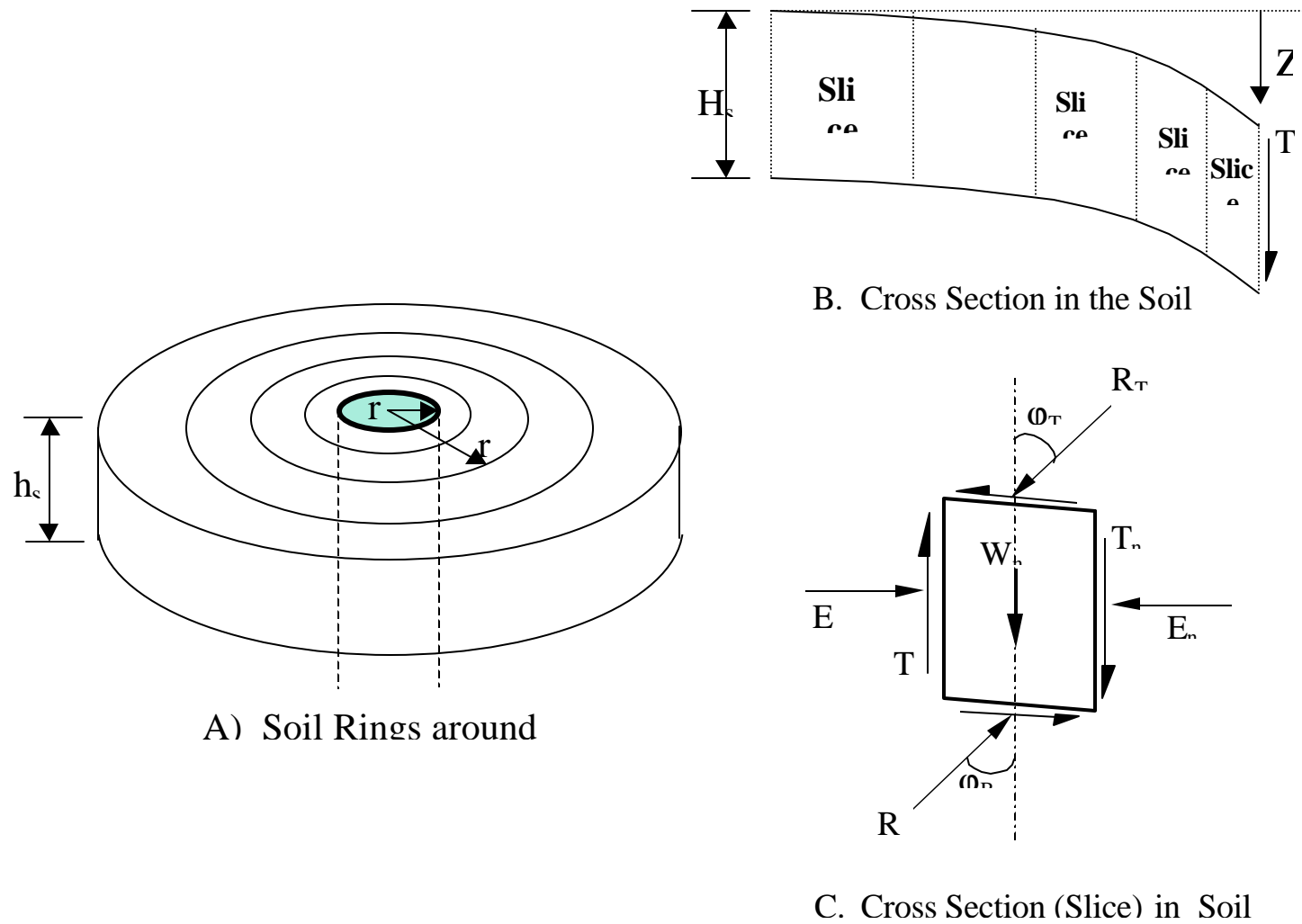


Fig. 4-10 Soil Rings Around the Pile and the Applying forces on Each Soil Ring (Slice)

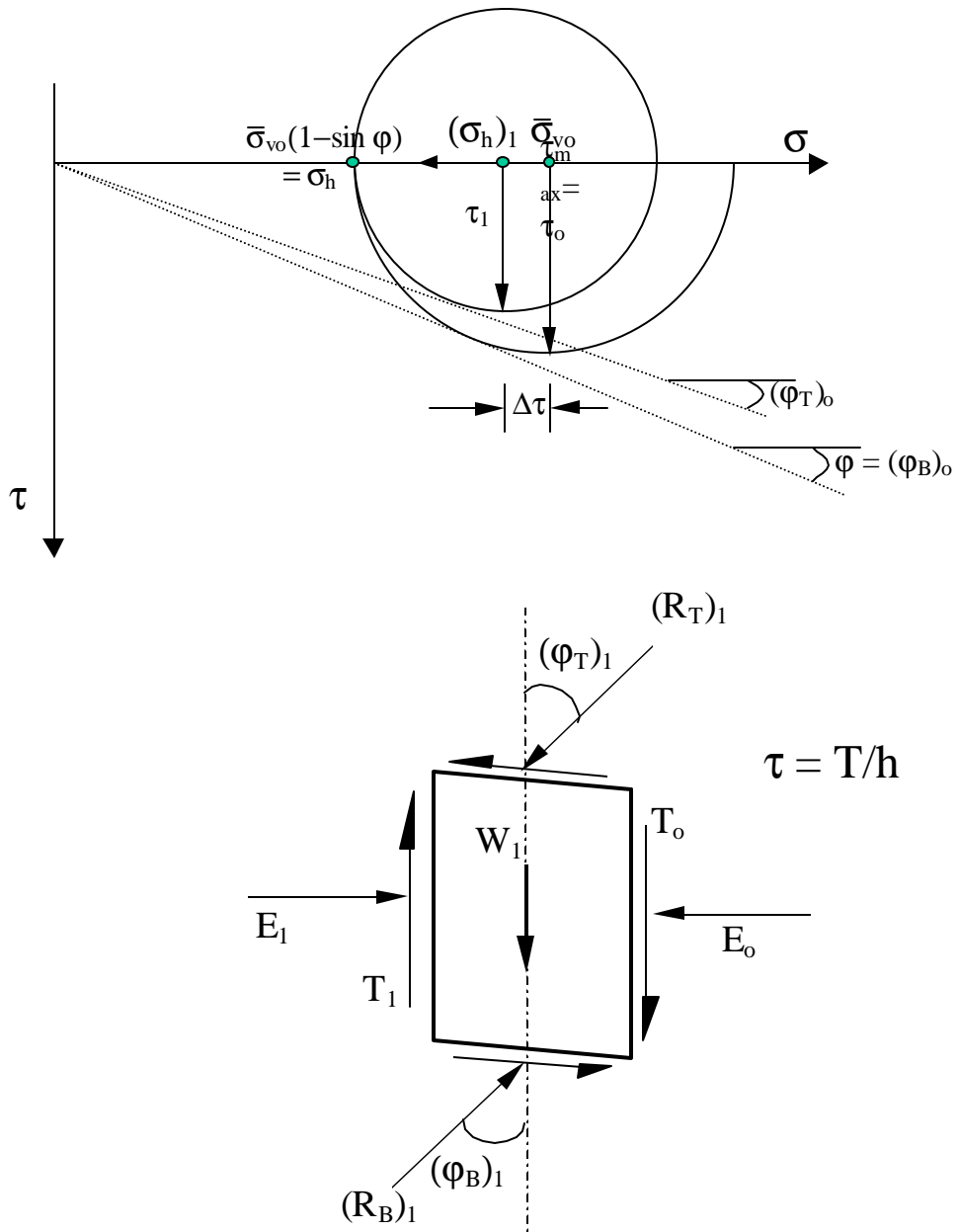


Fig. 4-11 Forces and Stresses Applied on the Soil Ring (Slice) Number 1

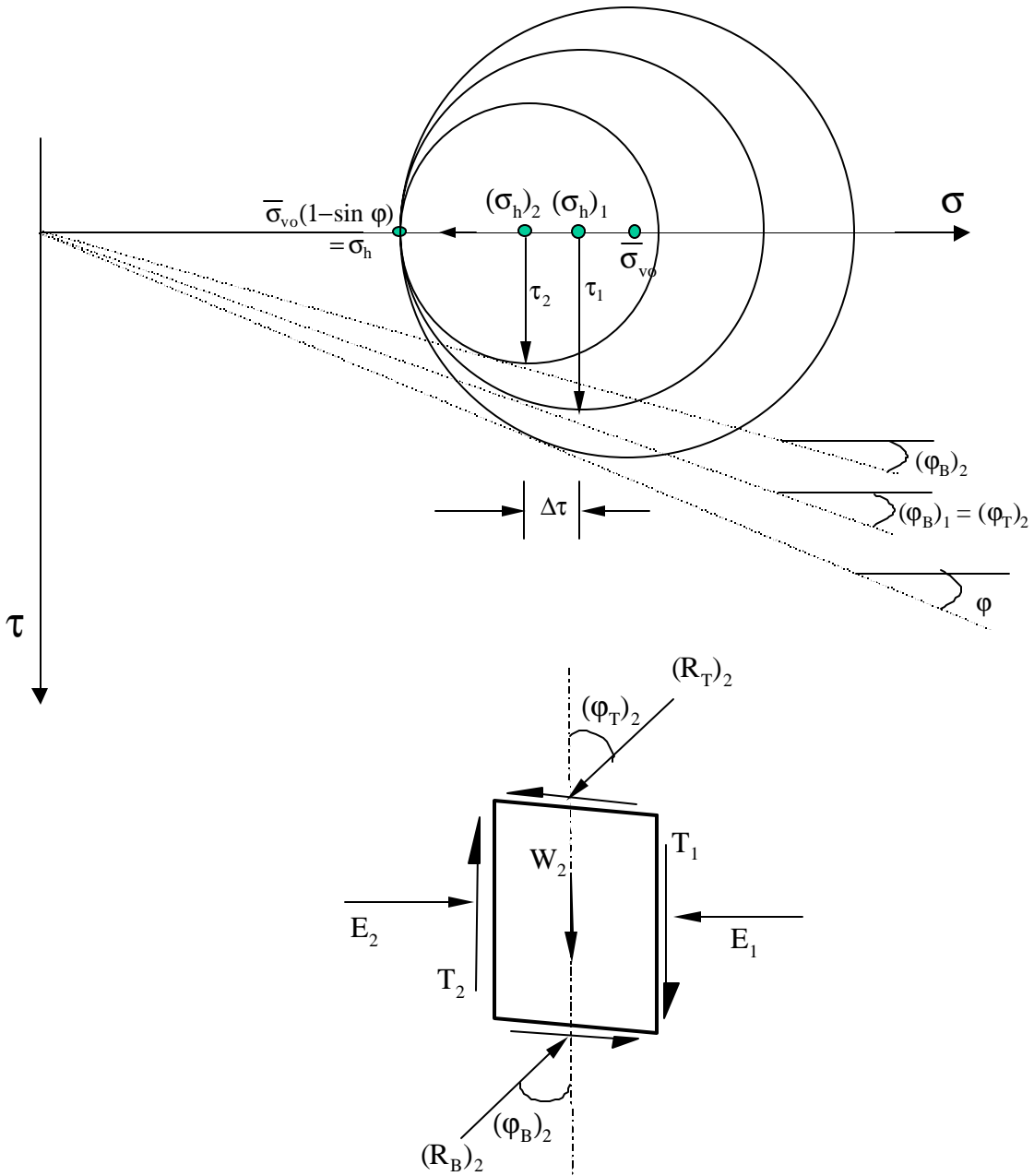


Fig. 4-12 Forces and Stresses Applied on the Soil Ring (Slice) Number 2

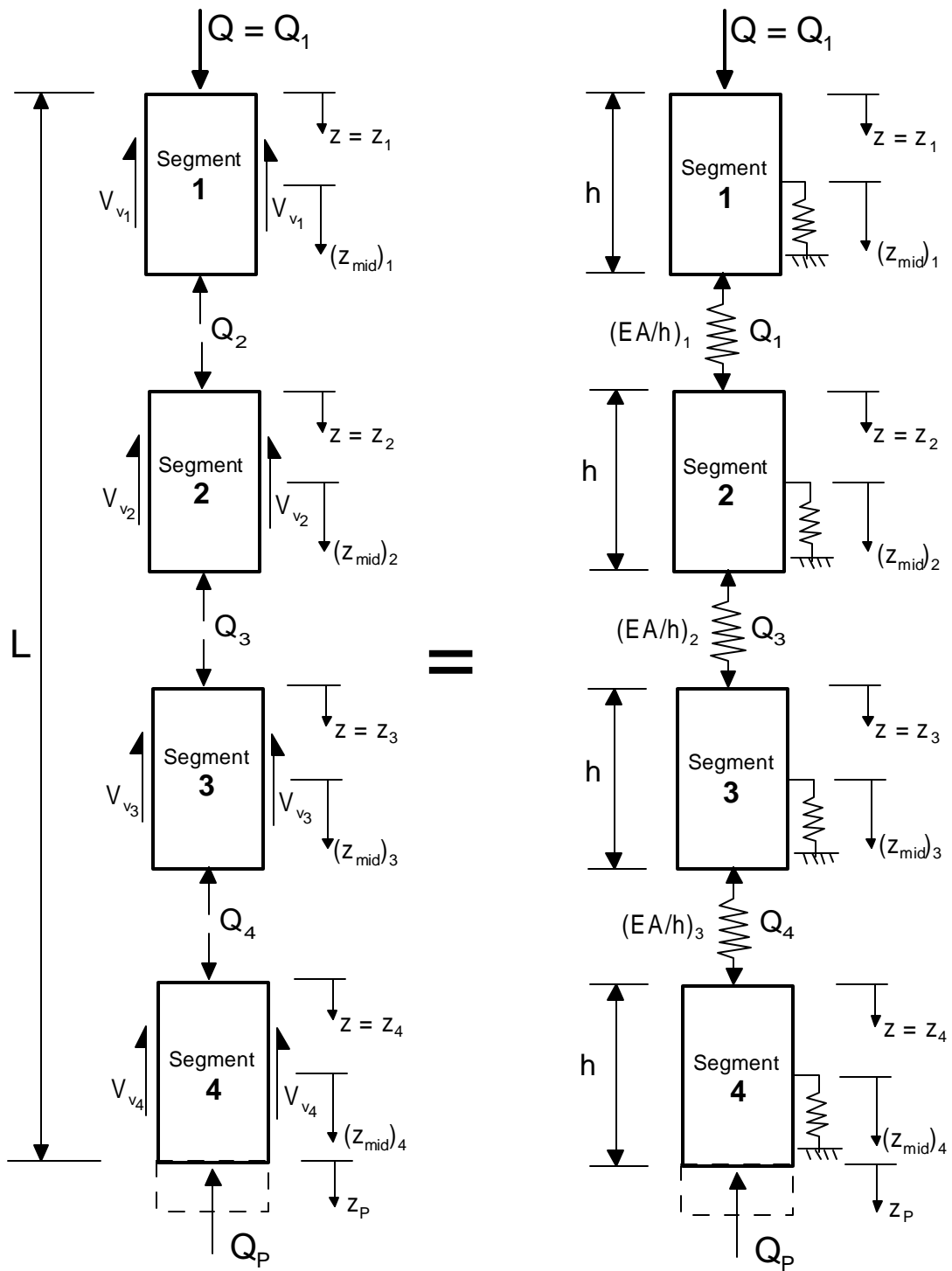


Fig. 4-13 Modeling Axially Loaded Pile Divided into Segments

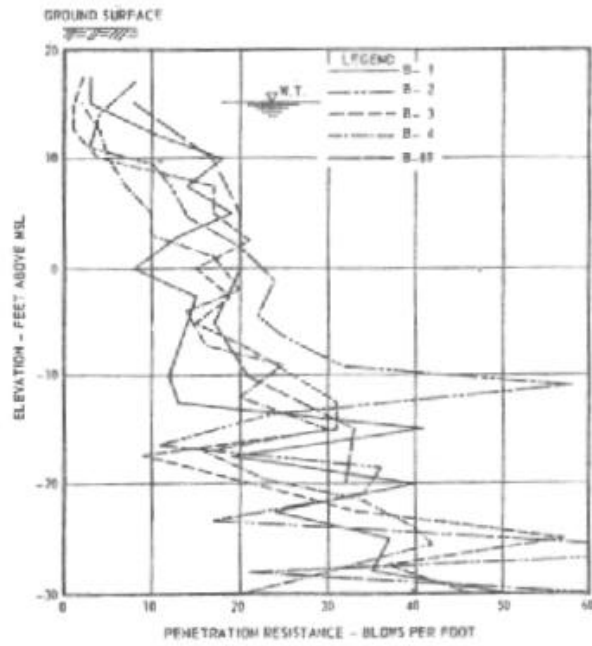


Fig. 4-14 Results of the Standard Penetration Tests (SPT) at Different Locations (Vesic, 1970)

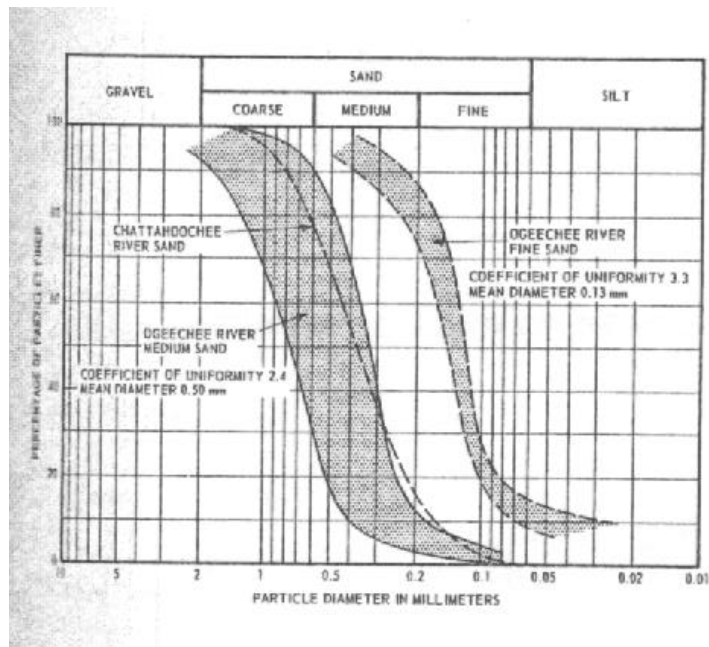


Fig. 4-15 Particle Size Distribution of Sands at Test Site

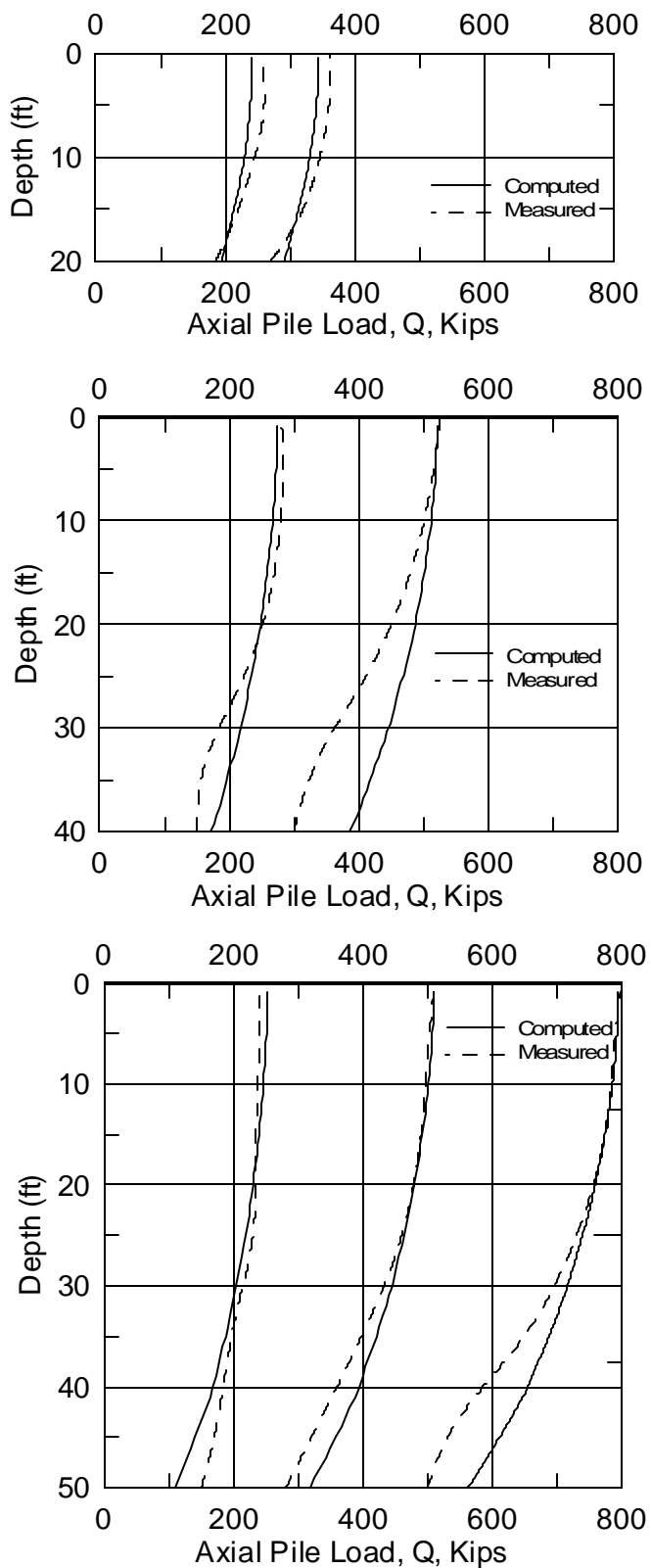


Fig. 4-16 A Comparison Between Measured and Computed Axial Pile Load at Different Depths (After Vesic, 1970)